Realization of dynamically controlled resonator pairs in nanomechanical arrays

Yichuan Zhang,[1,2] Tian Tian,[3,4] Shaochun Lin,[1,2] Jingwei Zhou,[1,2] Longhao Wu,[1,2] Zhouning Liu,[1,2] Chang-Kui Duan,[1,2] Liang Zhang,[1,2,5,*] and Jiangfeng Du[1,2,5]

[1] *Chinese Academy of Sciences (CAS) Key Laboratory of Microscale Magnetic Resonance and School of Physical Sciences, University of Science and Technology of China, Hefei 230026, China*

[2] *CAS Center for Excellence in Quantum Information and Quantum Physics, University of Science and Technology of China, Hefei 230026, China*

[3] *State Key Laboratory of Quantum Optics and Quantum Optics Devices, Institute of Opto-Electronics, Shanxi University, Taiyuan 030006, China*

[4] *Collaborative Innovation Center of Extreme Optics, Shanxi University, Taiyuan 030006, China*

[5] *Institute of Quantum Sensing and School of Physics, Zhejiang University, Hangzhou 310027, China*

(Received 20 February 2024; revised 2 July 2024; accepted 30 July 2024; published 22 August 2024)

Nanomechanical resonator arrays constitute a promising platform for topological physics and integrated acoustic devices. However, achieving precise control of the couplings between resonators has been a significant challenge for realizing a time-dependent Hamiltonian. In this work, we address this challenge by designing the geometric parameters of the resonators, enabling us to achieve dynamical control over the coupling strength and frequency stability. Our scalable resonator array allows for the dynamic control of coupling strengths between every individual resonator pair, ranging from zero to more than 20 times the dissipation rate. Moreover, we demonstrate Rabi-like oscillations with real-time-varying Rabi frequencies. This dynamically controlled system provides an extended platform for investigating dynamic processes and their applications.

DOI: 10.1103/PhysRevApplied.22.024060

I. INTRODUCTION

Nanomechanical resonator arrays are promising platforms for enhanced sensing [1,2], phonon transmission [3–5], quantum information processing [6], and the exploration of complex collective dynamics [7–10]. Dynamically controlled coupling involves arbitrary control of the coupling between resonators over time, encompassing periodic, quasiperiodic, or other forms of coupling control, thus broadening the applications of the array. This control enables topological pumping [11,12] and facilitates the creation of synthetic gauge fields [13]. Recently, researchers have achieved dynamic control over several modes in a single resonator [14,15] and over collective modes in a few resonators [16–18]. To further manipulate the coherent modes in a larger lattice, achieving dynamical couplings between discrete resonators presents a relatively simple approach. However, this remains a challenge in experiments.

Considerable progress has been made in tuning the coupling strengths through methods such as strain [19–21], the piezoelectric effect [22], and cavity coupling [23]. The electrostatic parametric coupled array [5,24] has attracted attention due to its scalability in forming extensive lattices and its ability to mitigate undesirable strain coupling. Furthermore, the strength of couplings is directly proportional to the adjustable ac voltage, facilitating precise reconfiguration of the couplings [25,26]. However, dynamic tuning of the coupling strength over a broad range can result in parametric coupling failures in experiments. Robust broad-range dynamic control requires the addressing of the complex interplay between couplings and resonance modes, as well as between coupling themselves, thereby imposing new requirements on the design of the geometry. A systematic analysis of coupling mechanisms is crucial for optimizing geometry design, ensuring the elimination of influencing factors and enhancing the system reliability.

In this paper, we conduct a comprehensive investigation into the electrostatic parametric coupling mechanism. Numerical results and experiments shed light on the role of the geometric parameters of the nanomechanical resonator array in determining the coupling strength and dissipation. We further explore the impact of control voltage on the coupling strengths and the frequency shifts of the resonators. We discover that the previous limitations in dynamically controlling electrostatically coupled arrays

*Contact author: liangzhang23@zju.edu.cn

[5,24] stem from the changing electrostatic force, which alters the resonant frequency of the mechanical resonator, leading to parametric coupling failure. We subsequently redesign the geometric parameters of the nanomechanical resonator array to enable a dynamically controllable coupling strength, ranging from zero to the highest possible value, thus achieving a balance between the coupling strength, dissipation, frequency stability, and fabrication yield. We showcase substantial control over the resonators by employing Rabi-like oscillations with variable oscillation frequencies in real time. This exemplifies the ability to continuously change the coupling strength without causing other changes during the experiment.

II. EXPERIMENTAL SYSTEM

We present the device in Fig. 1 and in Fig. 1(a) we outline the fabrication process, which consists of the following steps:

(i) A high-resistance silicon wafer is coated on both sides using low-pressure chemical vapor deposition (LPCVD) with a high-stress silicon nitride layer measuring 100 nm in thickness, exhibiting a tensile stress of $T_{\mathrm{SiN}} = 1$ GPa.

(ii) The lithography is followed by the evaporation of 10 nm of gold (Au) and 5 nm of chromium (Cr), followed by a lift-off process to create the metal layers. This process is reiterated to produce a thicker bonding area.

(iii) The contours of the string resonators are defined through electron-beam lithography (EBL), followed by inductively coupled plasma reactive-ion etching (ICP RIE) to etch the metal in the resonator gaps.

(iv) The RIE is followed by etching of the silicon nitride in the gap, while the surrounding areas are protected by photoresist and metal.

(v) The resonator array is rendered suspended through the application of potassium hydroxide (KOH) wet etching. Furthermore, focused-ion-beam (FIB) etching is used to eliminate intrinsic strain coupling by modifying the resonator clamping area. The modifications ensure that parametric couplings become predominant.

This array consists of several high-stress silicon nitride (SiN) suspended beams with dimensions of length l, width w, thickness h_1, and a gap d between the resonators, as shown in Fig. 1(b). In the linear regime, the double-clamped beams can be modeled as simple-harmonic resonators. The equivalent displacement of the ith resonator is z_i. Electrostatic parametric coupling between the resonators is achieved by applying a modulated voltage through external electrodes, which are connected to a metal coating of thickness h_2 on the resonators [24,27]. Furthermore, this metal coating facilitates the use of the standard magnetomotive technique for excitation and detection of the resonators [28].

In Fig. 1(c), we depict a schematic of the experimental circuits. A lock-in amplifier is connected to the resonator i, which excites and detects the motion of the resonator in an ambient magnetic field of 0.9 T along the Y direction. In order to couple the adjacent resonators, a voltage

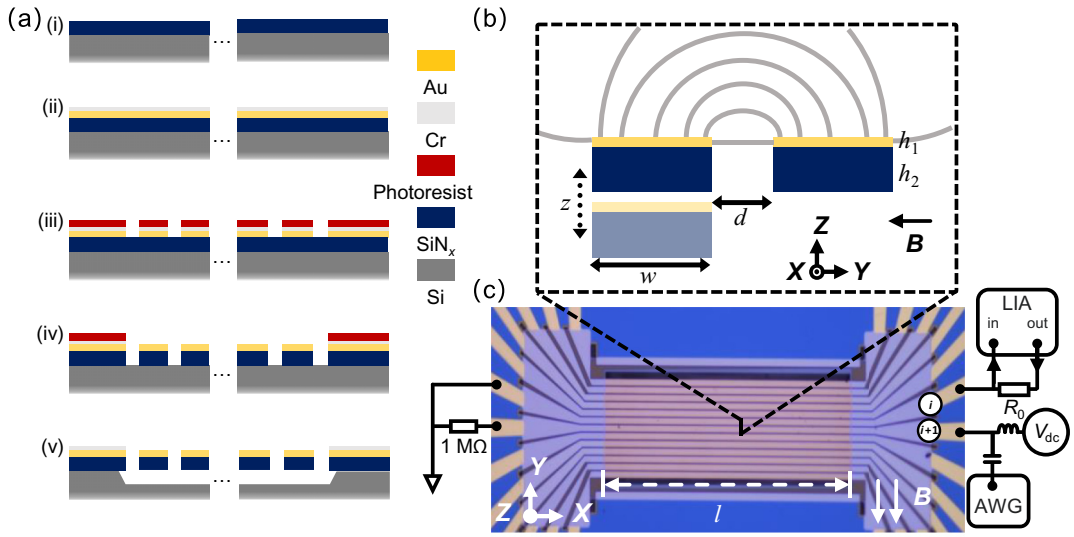

FIG. 1. The fabrication, coupling mechanism, and measurement circuit of the device. (a) The fabrication process of the Au-coated silicon nitride resonator array: (i) LPCVD; (ii) coating and lift-off; (iii) EBL and ICP; (iv) RIE; (v) wet etch (KOH). (b) A two-dimensional (2D) cross-section schematic of the coupled resonators, detailing the geometric parameters, including the width w, the gap d, and the thickness of the metal h_1 and SiN h_2, respectively. (c) A microscope image of the device, which consists of 13 double-clamped resonators, with dimensions of $l = 240$ μm, $w = 5$ μm, $d = 600$ nm, $h_1 = 20$ nm, and $h_2 = 100$ nm. The measurement circuit includes a lock-in amplifier (LIA), a dc source (V_{dc}) and an arbitrary waveform generator (AWG).

difference $V = V_{dc} + V_{ac}\cos(\nu_i^p t)$ is applied, where ν_i^p is the pumping frequency. The ac pumping from an arbitrary waveform generator (Zurich Instruments, HDAWG) and a dc voltage V_{dc} (Stanford Research Systems, SIM928) are combined via a bias tee connected to resonator $i+1$, while resonator i is grounded. The magnitude of the Z-direction component of the electrostatic force F_z is found to be directly proportional to the displacement difference between the resonators, $z = z_i - z_{i+1}$. Consequently, the relation $F_z \sim \zeta V^2 z = \partial F_z/\partial z \times z$ is derived, where ζ is the constant characterizing the electrostatic coupling between the resonators. Parametric coupling between the ith and $(i+1)$th resonators occurs when ν_i^p is equal to the difference in the resonance frequencies, $\nu_i^p = |\nu_i - \nu_{i+1}|$. The motion equations of the coupled resonators are derived as follows [24]:

$$\begin{cases} \ddot{z}_i + \gamma_i \dot{z}_i + \nu_i^2 z_i = 2g\cos(\nu_i^p t) z_{i+1}, \\ \ddot{z}_{i+1} + \gamma_{i+1}\dot{z}_{i+1} + \nu_{i+1}^2 z_{i+1} = 2g\cos(\nu_i^p t) z_i, \end{cases} \tag{1}$$

where γ_i is the dissipation rate, m indicates the uniform mass of the resonators, and $g = \zeta V_{dc} V_{ac}/m$ is the parametric coupling strength. The response spectrum of the resonator is analyzed using the lock-in amplifier (Zurich Instruments, HF2LI) and exhibits distinct peak splitting under conditions of strong coupling [for details, see Fig. 6(a) in Appendix C]. The width of the peak splitting Ω is directly correlated with the strength of coupling,

$$\Omega = g/\sqrt{\nu_i \nu_{i+1}}. \tag{2}$$

III. ANALYSES

The coupling mechanism is analyzed by finite-element analyses (FEAs) and experimental measurements. The electrostatic force is proportional to the length l. To assess the dependence of the coupling strength on the geometric parameters of the array, FEA in two dimensions is then utilized, as illustrated in Fig. 1(b) (for details, see Appendix A). F_z maintains a linear relationship with the relative displacement along the Z axis, enabling the fitting of $\zeta/l = (\partial F_z/\partial Z)/(lV^2)$ [Fig. 2(a), inset]. The parameter ζ/l serves as a metric to quantify the coupling capacity of the resonator array in terms of the geometric parameters, excluding the length.

In Fig. 2(a), we illustrate a significant decrease in the coupling coefficient ζ/l as the gap distance d decreases. The influence of the width on ζ/l is relatively minor in comparison to that of d, particularly when $w > d$. A power-law fit of $\zeta/l \propto (d/d_0)^{-\alpha}$ is observed, where α is fitted to 1.826 and d_0 is the unit gap distance. The coupling coefficients are calculated from the slope of the linear fitting of the Z-direction electromagnetic force F_z at differing amplitudes per unit length per unit voltage, as shown in the inset. In Fig. 2(b), we observe a linear increase of the coupling coefficient ζ/l with variations of

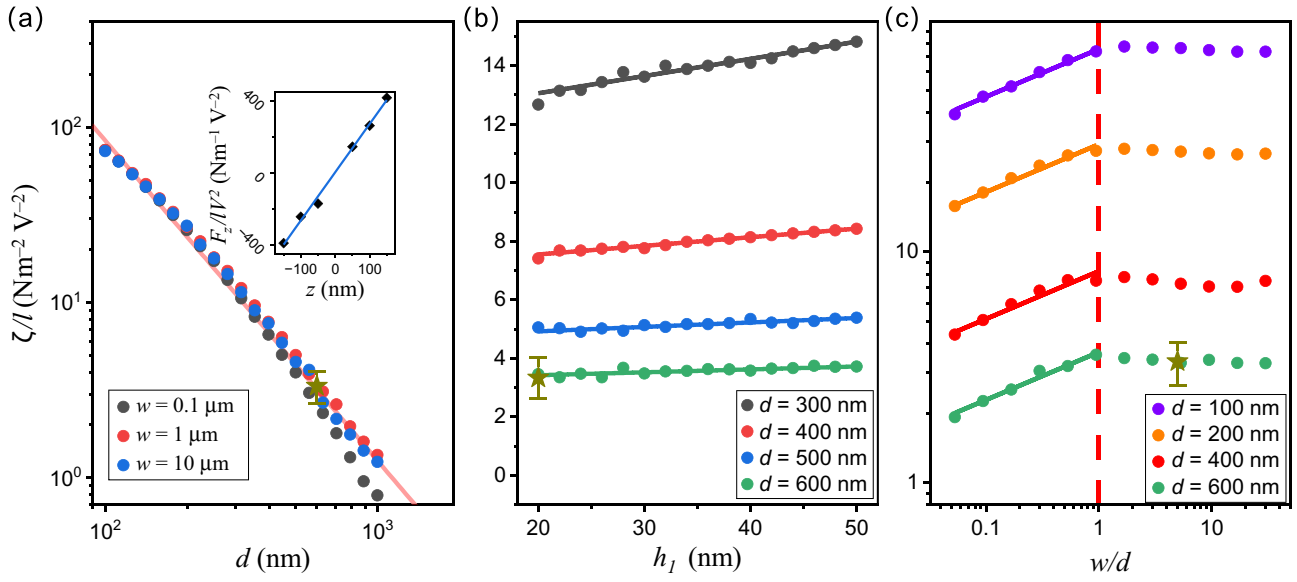

FIG. 2. The relationship between the coupling coefficient ζ/l and the geometric parameters. The dark yellow star represents the measured mean coupling strength of the array shown in Fig. 1. (a) The numerical results of ζ/l versus the gap d, where the width $w = 0.1, 1, 10$ μm and the thickness of the metal layer $h_1 = 20$ nm. The red line shows the exponential fitting. The inset illustrates the linear fitting of $(\partial F_z/\partial z)/(lV^2)$, with coupling coefficient ζ/l. (b) The results of ζ/l versus the thickness of the metal layer h_1, with width $w = 5$ μm and the gap d ranging from 300 to 600 nm. The lines show the results of a linear fit. (c) The impact of varying the width gap ratio w/d with $h_1 = 20$ nm and d from 100 to 600 nm. The solid lines show that ζ/l grows exponentially with w when $w/d < 1$. The dashed line guides the turning points at $w/d = 1$ and ζ/l is unchanged with w when $w/d > 1$.

h_1, $\zeta/l \propto (h_1 + h_0)$, where the fitting intercept h_0 is different for differing gaps d. In Fig. 2(c), we show the impact of the width with the aspect ratio, where a marked change occurs at $w/d = 1$. For $w/d < 1$, the coupling coefficient increases exponentially with the width, following the fit $\zeta/l \propto (w/w_0)^{\beta}$, with $\beta = 0.220$. However, when $w/d > 1$, the coupling coefficient remains nearly unchanged, leading to $\zeta/l \propto (d/d_0)^{-\alpha}(h_1 + h_0)$. The turning points occur at $w/d = 1$, with differing gaps d. When $w/d > 1$, we can characterize the coupling strength g (for details, see Appendix C) as follows:

$$\begin{cases} g \propto \left(\dfrac{d}{d_0}\right)^{-\alpha} \times \dfrac{h_1 + h_0}{(\rho_1 h_1 + \rho_2 h_2)w} V_{\mathrm{dc}} V_{\mathrm{ac}}, \\ \Omega \propto l \left(\dfrac{d}{d_0}\right)^{-\alpha} \times \dfrac{h_1 + h_0}{\sqrt{\rho A T_{\mathrm{SiN}}}} V_{\mathrm{dc}} V_{\mathrm{ac}}. \end{cases} \tag{3}$$

Here, $\rho_{1,2}$ denotes the equivalent density of the metal and silicon nitride layers and T_{SiN} signifies the stress in the silicon nitride layer.

In addition to enhancing the coupling strength, it is also important to minimize the dissipation in the resonators. A quantitative investigation has been conducted into the relationship between the geometric parameters and the resonator dissipation.

In experiments, the total dissipation γ can be expressed as $\gamma = \gamma_{\mathrm{mag}} + \gamma_{\mathrm{cl}} + \gamma_0$, where γ_{mag} represents the magnetomotive dissipation [28] and γ_{cl} is the clamping loss [29]. γ_0 represents the sum of the remaining dissipation, including the multilayer loss [30], the thermoelasticity [31,32], the phonon interaction [33,34], and the gas damping [35]. The dissipation factors listed above have no obvious relationship with the length l and width w of the beam when the thicknesses h_1 and h_2 are determined. Therefore, we mainly consider the competition between the magnetic dissipation and the clamping loss.

The total dissipation γ of beams of differing geometries is measured at room temperature, as shown by the black dots in Fig. 3(a). The magnetomotive dissipation comes mainly from the measurement circuits. The excitation and readout of the resonator, which are based on the Lorentz force and the electromotive force, are modeled as an *RLC* parallel circuit with characteristic impedance $Z_c = \xi l^2 B^2/(m\nu)$ [28]. ξ is a constant relating to the beam shape and B is the uniform ambient magnetic field. The magnetomotive dissipation, γ_{mag}, is derived as $\gamma_{\mathrm{mag}} = \nu Z_c R_{\mathrm{ext}}/|Z_{\mathrm{ext}}|^2 \propto B^2 l w^{-1}$. The terms R_{ext} and Z_{ext} denote the resistance and impedance of the external measurement circuit, respectively. Calibration of the coefficient $R_{\mathrm{ext}}/|Z_{\mathrm{ext}}|^2$ involves measuring the dissipation as a function of the magnetic field (for details, see Appendix B). Furthermore, γ_{mag} for various aspect ratios is depicted by the blue line in Fig. 3(a) and the blue triangle indicates the experimental results.

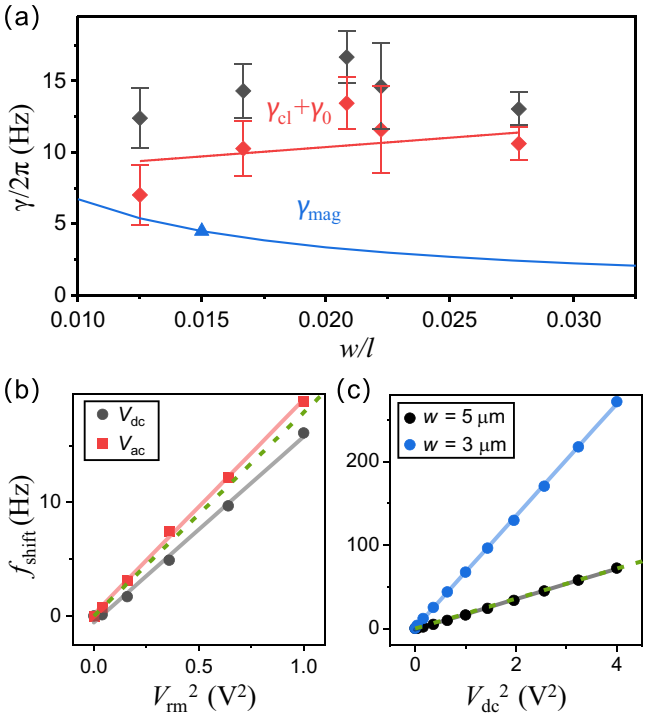

FIG. 3. The influence of the geometry on the dissipation and the resonance frequency. (a) The dissipation γ versus the aspect ratio w/l, with ambient magnetic field $B = 0.9$ T. The black dots are the measured mean dissipation of the resonators in differing array samples. The blue triangle is the measured magnetomotive dissipation, from the calibration of the varying magnetic field (the error bar is smaller than the triangle). The blue line is an extension of the result. The red dots represent the dissipation excluding the magnetomotive dissipation, $\gamma - \gamma_{\mathrm{mag}} = \gamma_{\mathrm{cl}} + \gamma_0$, and the red line is a linear fit. (b) The experimentally measured frequency shift caused by the applied V_{dc} and V_{ac}. $V_{\mathrm{rm}}^2 = V_{\mathrm{dc}}^2 = V_{\mathrm{ac}}^2/2$, with the width of resonator being $w = 5$ μm. The lines are fitting results and the dashed line is the theoretical result. (c) The measured frequency shifts caused by the voltage applied to the resonators, V_{dc}, with $w = 3, 5$ μm. The lines are the fitting results and the dashed line is the theoretical result.

The dissipation arising from the elastic energy radiation through the supports into the substrates is known as the clamping loss and is characterized by $\gamma_{\mathrm{cl}} \propto w/l$ [29]. $\gamma_{\mathrm{cl}} + \gamma_0$ can be obtained as $\gamma - \gamma_{\mathrm{mag}}$, as shown by the red dots in Fig. 3(a). The red line is the result of a linear fitting. According to the above analysis, the relationship between the total dissipation and the aspect ratio is obtained, $\gamma = P_{\mathrm{mag}} l/w + P_{\mathrm{cl}} w/l + \gamma_0$. The values of the coefficients are derived from the fitting: $P_{\mathrm{cl}} = 2\pi \times (136 \pm 166)$ (Hz), $P_{\mathrm{mag}} = 2\pi \times (0.0672 \pm 0.0019)$ (Hz), and $\gamma_0 = 2\pi \times (7.89 \pm 2.98)$ (Hz).

Another issue that must be considered is the effect of the control voltages on the resonance frequencies of the resonators, because a key feature of the parametric coupling method is the frequency selectivity. First, the resonance frequency shift $\Delta\nu_i = \nu_i - \tilde{\nu}_i$ resulting from the

electrostatic force is delineated in Appendix C,

$$\Delta\nu_i \approx \zeta \frac{V_{\rm dc}^2 + V_{\rm ac}^2/2}{2m\tilde{\nu}_i}. \tag{4}$$

In Fig. 3(b), we display the experimentally measured frequency shift, with an independently applied $V_{\rm dc}$ or $V_{\rm ac}$. It should be noted that the horizontal axis represents the mean square value of the voltage, $V_{\rm rm}^2$. The geometric parameters of the resonators are as follows: $l = 240$ μm, $w = 5$ μm, $d = 600$ nm, and $h_1 = 20$ nm. Through the FEA, we obtain that $\Delta\nu/V_{\rm rm}^2 \approx 2\pi \times 17.92\ {\rm Hz\,V^{-2}}$, which is in good agreement with the experiments, as shown in Fig. 3(b).

In Fig. 3(c), we illustrate the effect of resonators of differing widths on the frequency shift. As the width decreases, there is a notable increase in the frequency shift, even though the electrostatic force $F_z = \zeta V^2 z$ is almost the same. This suggests that when the width is large (such as 5 μm), the electrostatic force F_z is the primary source causing the frequency shift, coinciding well with the theoretical calculation. However, when the width is small, some nonobvious factors dominate. In order to minimize the frequency shift, fabricating the resonators with a larger width is imperative. In addition, since the coupling strength scales with $V_{\rm dc}V_{\rm ac}$, actively increasing $V_{\rm dc}$ and decreasing the $V_{\rm ac}$ contributes to the control stability of the coupling strength over time. Widening the beam could enhance its tolerance to high $V_{\rm dc}$. This method proves effective in mitigating frequency shifts during the experiments. Extensive fabrication and measurement results of array samples demonstrate that for lengths within $l \in [180, 240]$ μm, a width larger than 5 μm is crucial to ensure that the frequency shift from nonelectrostatic force factors is insignificant, thus facilitating real-time resonator control.

IV. RESULTS

The nanomechanical resonator array, featuring dimensions of $l = 240$ μm, $w = 5$ μm, $d = 600$ nm, $h_1 = 20$ nm, and $h_2 = 100$ nm, exhibits high fabrication yields, enabling the creation of arrays comprising up to more than ten consecutive resonators. At 77 K and within a 0.9 T magnetic field, the eigenfrequency of the resonators stands at approximately 770 kHz and their Q factors typically exceed 6×10^4. The electrostatic coupling strength demonstrates a linear relationship with $V_{\rm dc}$ and $V_{\rm ac}$ (for details, see Appendix C). The characterization of a typical array with ten resonators is shown in Table I. The average $\zeta/l = 3.34 \pm 0.70\ ({\rm Nm^{-2}\,V^{-2}})$ is depicted as the dark yellow star in Fig. 2. The quantitative design of such geometric parameters yields a coupling parameter of $\zeta/l = 3.46\ ({\rm Nm^{-2}\,V^{-2}})$, which aligns with the experimental findings. Furthermore, Table I reports that all nearest-neighbor coupling between adjacent resonators could be tuned from 0 to 20γ, greatly expanding the applications of this array.

TABLE I. Characterization of the coupling strength. The coupling strength is linearly proportional to the product $V_{\rm dc}V_{\rm ac}$. The coefficients ζ for the nearest-neighbor coupling strength for an array of ten resonators are listed. $\Omega_{\rm max}$ is the split when $V_{\rm ac} = 0.8$ V and $V_{\rm dc} = 9.5$ V.

$i, i+1$	$\zeta/m\nu$ (Hz V^{-2})	$\Omega_{\rm max}/\gamma$
1,2	33.50	27.19
2,3	35.55	33.48
3,4	25.41	23.21
4,5	31.27	23.58
5,6	48.03	36.54
6,7	27.63	22.13
7,8	38.91	30.78
8,9	31.02	23.34
9,10	41.39	30.72

The behavior of the coupled classical mechanical resonators can be analogous to the Schrödinger equations (for details of the analogy, see Appendix D). The transfer

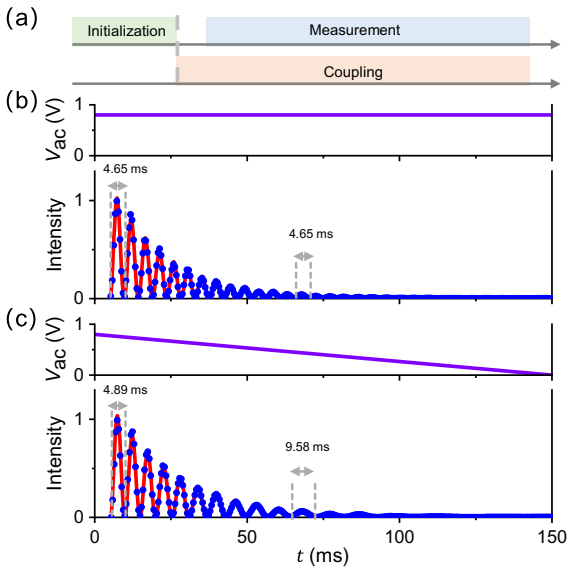

FIG. 4. The demonstration of Rabi-like oscillations of the vibration intensity of the resonator. (a) The measurement sequence. (b),(c) The upper parts depict the values of the applied $V_{\rm ac}$ throughout the measurement, corresponding to the variation of the coupling strength. The lower parts illustrate the experimentally measured vibration intensity (blue points). The red line is fitted according to Rabi-like oscillations. The error bars are smaller than the data points. $t = 77K$ and $V_{\rm dc} = 8$ V. (b) $V_{\rm ac} = 0.8$ V, yielding a constant coupling strength. The Rabi-like oscillations have constant periods, $T_R = 4.65$ ms. (c) $V_{\rm ac} = 0.8(1 - t/150)$ (V). The periods of the Rabi-like oscillations vary from about $T_R = 4.89$ ms to more than 9.58 ms.

of elastic energy between coupled resonators can be explained in a form similar to Rabi oscillation [20,22]. In Fig. 4, we illustrate such oscillations and demonstrate the dynamic control of the coupling strength. The experiment sequence is shown in Fig. 4(a). Resonator i is excited to a steady-state vibration. Then, $V_{\rm dc}$ and $V_{\rm ac}$ are applied to resonator $i+1$ to turn on the parametric coupling between the adjacent resonators. Meanwhile, the excitation is turned off and the vibration intensity is measured on resonator i. The oscillations of the coherently transferred elastic energy are observed. The oscillation frequency serves as a probe for the coupling strength. It is crucial to note that throughout this process, there is no occurrence of quantum state superposition or entanglement.

In Fig. 4(b), $V_{\rm ac}$ is maintained at a constant value throughout the measurement, so that the oscillation period remains constant. The normalized signal intensity can be fitted by $V_S \sim e^{-\gamma t}\cos^2(\Omega t/2)$, where $\gamma/2\pi = 8.56$ Hz represents the dissipation and $\Omega/2\pi = 1/T_R = 215$ Hz. As shown in Fig. 4(c), a continuously varying $V_{\rm ac}$ may induce variations in the coupling strength, resulting in the coupling strength being dynamically reduced from more than 20γ to 0. $V_s(t)$ is fitted as $e^{-\gamma t}\cos^2\{(\Omega t/2)[1-(t/2T)]\}$, where $T = 150$ ms is the total time. These period-varying oscillations exemplify real-time control over each coupling strength in the whole array.

V. CONCLUSIONS

In conclusion, we have numerically and experimentally analyzed the effects of the geometric and control parameters on the coupling strength, dissipation, and frequency shift of nanomechanical resonator pairs. Based on these studies, we have successfully developed a nanomechanical resonator array featuring dynamical-control capabilities. *In situ*, real-time, and wide-ranging control of the coupling strength is demonstrated via Rabi-like oscillations with a time-varying Rabi frequency. This array enables the construction and observation of arbitrarily time-dependent processes in the lattice. Promising applications are expected in the fields of topological adiabatic and nonadiabatic transfer of coherent phonons [36,37]. Furthermore, this array can be used to construct a quasi-one-dimensional system for the experimental study of quasiperiodic physics [38] and the multidimensional gauge field [39].

ACKNOWLEDGMENTS

This work was supported by the National Key R&D Program of China (Grants No. 2021YFB3202800 and 2023YFB3209900), the National Natural Science Foundation of China (Grants No. T2388102, No. 12304566, and No. 12205191), the Fundamental Research Funds for the Central Universities (Grant No. 226-2023-00139), and the Fundamental Research Program of Shanxi Province (Grant No. 202303021221067). This work was partially carried out at the University of Science and Technology of China (USTC) Center for Micro- and Nanoscale Research and Fabrication. We acknowledge engineers W. Liu, Y. Ye, and W. Li for their assistance during sample fabrication.

APPENDIX A: SIMPLIFYING THE ELECTROSTATIC FORCE CALCULATIONS INTO TWO DIMENSIONS

The coupled resonators are akin to slightly staggered parallel-plate capacitors. Previous FEAs have explored the properties of parallel-plate capacitors [40,41]. The electrostatic force exerted on the slightly staggered resonator beams can be calculated using the Maxwell stress-tensor method [42]. Under the conditions that the length is much larger than the width and thickness of resonators, $l \gg w, h$, edge effects along the X axis can be neglected, implying $E_x \approx 0$ and thus allowing for the neglect of the tensor $\overleftrightarrow{T}$ associated with the X axis. Consequently, the length l can be extracted from the integral

$$F = \oint_s \overleftrightarrow{T} dA = l \oint \overleftrightarrow{T}_{\rm 2D} ds, \tag{A1}$$

where the symbol s denotes the surface of the resonator, with the integral being taken over this surface. $\overleftrightarrow{T}_{\rm 2D}$ signifies the Maxwell stress tensor in the Y-Z plane and the integral is computed around the cross section.

APPENDIX B: CALIBRATION OF MAGNETO-MOTIVE DAMPING

The oscillator drive and measurement based on electromagnetic induction can be equated to an RLC parallel circuit with the impedance $Z_c = \xi l^2 B^2/(m\nu)$ of the oscillator [28], where ξ is a geometry constant, B is the strength of the applied magnetic field, l is the length of the resonator, m is the mass, and ν is the resonance frequency of the fundamental vibration mode. $R_{\rm ext}$ and $Z_{\rm ext}$ are, respectively, the resistance and complex impedance of the external circuit used for excitation and measurement:

$$\gamma_{\rm mag} = \frac{\nu Z_c R_{\rm ext}}{|Z_{\rm ext}|^2} = \frac{\xi R_{\rm ext}}{|Z_{\rm ext}|^2}\frac{l}{(h_1\rho_1 + h_2\rho_2)w}B^2 \propto B^2. \tag{B1}$$

Here, $\xi R_{\rm ext}/|Z_{\rm ext}|^2$ can be calibrated by measuring the dissipation versus the magnetic field, at the ambient temperature of 4 K, as shown in Fig. 5. It is noted that the magnetomotive damping is independent with temperature.

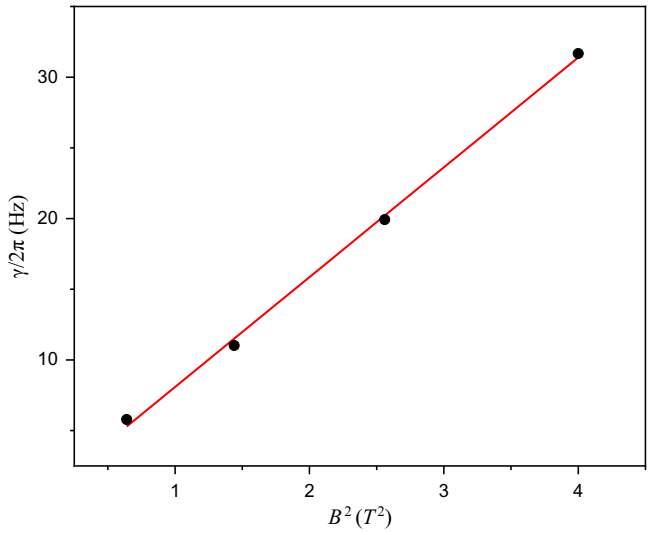

FIG. 5. The calibration of the magnetomotive damping. The dissipation has been measured as a function of variable magnetic fields (B^2) using experimental circuits at a temperature of 4 K. The length of the resonator is $l = 200$ nm and the width is $w = 3$ nm. The dissipation increases linearly with B^2 and the slope is fitted to be 7.769 (Hz/T^2).

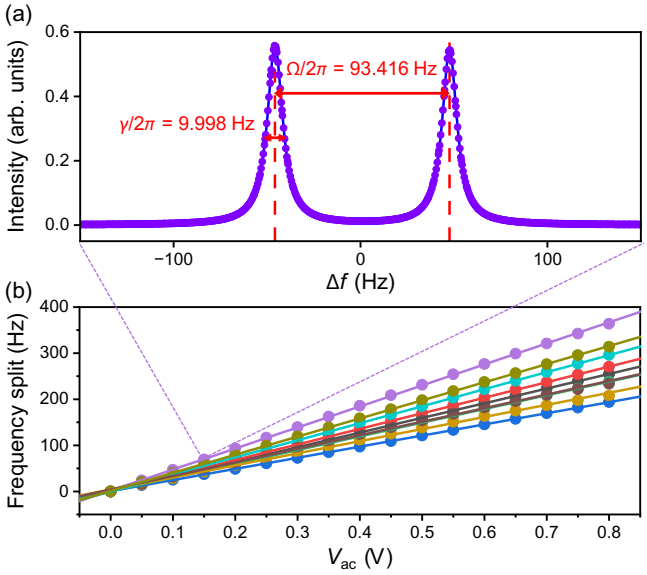

FIG. 6. The characterization of the coupling strength. (a) The frequency response spectrum is measured with $V_{dc} = 9.5$ V and $V_{ac} = 0.2$ V applied across resonators 5 and 6. (b) The frequency split of the array of ten resonators as a function of V_{ac}, with $V_{dc} = 9.5$ V. The frequency of the ac pumping signal does not change during the variation of V_{ac}. The frequency split exhibits a linear relationship with V_{ac}.

APPENDIX C: CHARACTERIZATION OF THE COUPLING STRENGTH OF RESONATOR PAIRS

Consider the equations of motion of coupled adjacent resonators S and I [24] with applied drive $F_D e^{i\nu_D t}$,

$$\begin{cases} \ddot{z}_S + \gamma_S \dot{z}_S + \tilde{\nu}_S^2 z_S = \dfrac{\zeta V^2}{m}(z_I - z_S) + \dfrac{F_D e^{i\nu_D t}}{m}, \\ \ddot{z}_I + \gamma_I \dot{z}_I + \tilde{\nu}_I^2 z_I = \dfrac{\zeta V^2}{m}(z_S - z_I). \end{cases} \tag{C1}$$

Here, $\gamma_{S,I} = \nu_{S,I}/Q_{S,I}$ are the decay rates and Q is the quality factor. As illustrated in Fig. 6, $\gamma/2\pi$ represents the full width at half maximum (FWHM) of the response spectrum, denoting average decay, $\gamma = \sqrt{\gamma_S \gamma_I}$. Substituting $V = V_{dc} + V_{ac}\cos(\nu^p t)$ into Eq. (C1) and performing the rotating-wave approximation yields

$$\begin{cases} \ddot{z}_S + \gamma_S \dot{z}_S + \nu_S^2 z_S = 2g\cos(\nu^p t) z_I + f_D e^{i\nu_D t}, \\ \ddot{z}_I + \gamma_I \dot{z}_I + \nu_I^2 z_I = 2g\cos(\nu^p t) z_S, \end{cases} \tag{C2}$$

where $g = \zeta V_{dc} V_{ac}/m$ denotes the coupling strength and the resonance frequencies of the fundamental modes of the resonators are shifted because of the applied electrostatic force,

$$\begin{aligned} \nu_{S,I} &= \sqrt{\tilde{\nu}_{S,I}^2 + \zeta \frac{V_{dc}^2 + V_{ac}^2/2}{m}}, \\ \Delta\nu = \nu - \tilde{\nu} &\approx \frac{\nu^2 - \tilde{\nu}^2}{2\tilde{\nu}} = \zeta \frac{V_{dc}^2 + V_{ac}^2/2}{2m\tilde{\nu}}. \end{aligned} \tag{C3}$$

Parametric coupling occurs when the pump frequency ν^p equals the difference in the shifted resonance frequencies, $\nu^p = |\nu_S - \nu_I|$. The $\cos(2\nu^p t)$ terms are neglected due to the rotating-wave approximation, $f_D = F_D/m$.

We use the Fourier-transform method to obtain the response of the resonators in the frequency domain:

$$\begin{cases} (\nu_S^2 - \nu^2 + i\nu\gamma_S)\chi_S[\nu] = g\chi_I[\nu - \nu^p] + f_D[\nu], \\ (\nu_I^2 - \nu^2 + i\nu\gamma_I)\chi_I[\nu] = g\chi_S[\nu - \nu^p]. \end{cases} \tag{C4}$$

Therefore,

$$\chi_S = \frac{f_D}{(\nu_S^2 - \nu^2 + i\nu\gamma_S) - \frac{g^2}{\nu_I^2 - (\nu+\nu^p)^2 + i(\nu+\nu^p)\gamma_I}}. \tag{C5}$$

We obtain two resonance frequencies near ν_S in the parametric coupled pairs under the conditions $\gamma_{S,I} \ll \nu^p \ll \nu_{S,I}$,

$$\nu_\pm \approx \nu_S \pm \frac{\Omega}{2}, \quad \Omega = \frac{g}{\sqrt{\nu_S \nu_I}}. \tag{C6}$$

The practice coupling strength g can be obtained by measuring the peak splitting width $\Delta\nu$ of the response spectrum, $\Delta\nu = \Omega = g/\sqrt{\nu_S \nu_I}$, as shown in Fig. 6(a).

For a high-stress double-clamped resonator, the resonant frequency of the fundamental mode is derived as

TABLE II. The measured resonance frequencies and Q factors of ten resonators in an array.

i	$\nu/2\pi$ (kHz)	Q
1	752.589	63 243
2	756.667	66 374
3	749.413	62 451
4	734.569	62 252
5	746.227	58 758
6	757.777	66 472
7	744.841	63 122
8	758.887	65 990
9	753.245	66 074
10	763.773	62 604

$\nu = \frac{1}{2l}\sqrt{T_{\mathrm{SiN}}/\rho A}$ [43], where $\rho A = w(\rho_1 h_1 + \rho_2 h_2)$. Here, $\rho_{1,2}$ and $h_{1,2}$ denote the equivalent density and thickness of the metal and silicon nitride layers, respectively. T_{SiN} represents the prestress in the silicon nitride layer. As shown in Table II, the frequencies and quality factors of the fabricated resonators are nearly uniform, so $m\sqrt{\nu_S \nu_I} \approx m\nu = \sqrt{\rho A T_{\mathrm{SiN}}}/2$ under the condition $\nu_S \approx \nu_I$. Based on the fitting results of Figure 2, we find that $\zeta/l \propto (d/d_0)^{-\alpha}(h_1 + h_0)$. The relation between the coupling strength g (peak splitting Ω) and the resonator geometry can be derived as

$$g = \frac{\zeta V_{\mathrm{dc}} V_{\mathrm{ac}}}{m} \propto \left(\frac{d}{d_0}\right)^{-\alpha} \times \frac{h_1 + h_0}{\rho A} V_{\mathrm{dc}} V_{\mathrm{ac}}, \tag{C7}$$

$$\Omega = \frac{g}{\sqrt{\nu_S \nu_I}} \propto l\left(\frac{d}{d_0}\right)^{-\alpha} \times \frac{h_1 + h_0}{\sqrt{\rho A T_{\mathrm{SiN}}}} V_{\mathrm{dc}} V_{\mathrm{ac}}. \tag{C8}$$

APPENDIX D: THE RABI-LIKE OSCILLATION IN COUPLED MECHANICAL RESONATOR PAIRS

Consider the equation of motion of the ith resonator in the lattice [24],

$$\ddot{z}_i + \gamma_i \dot{z}_i + \nu_i^2 z_i = 2g_{i-1}\cos(\nu_{i-1}^{\mathrm{p}} t) z_{i-1} + 2g_i \cos(\nu_i^{\mathrm{p}} t) z_{i+1}, \tag{D1}$$

where g_i denotes the coupling between the ith and $(i+1)$th resonators and the pump frequency $\nu_i^{\mathrm{p}} = |\nu_i - \nu_{i+1}|$. Taking the vibration phase into consideration, the complex amplitude ψ_i of the ith resonator is defined as

$$z_i(t) = \Re(\psi_i), \quad z_i(t) = \psi_i e^{i\nu_i t} + \psi_i^* e^{-i\nu_i t}. \tag{D2}$$

The complex amplitude can be measured by the lock-in amplifier, $\psi_i = |\psi_i(t)| e^{i\theta_i(t)}$, where $\theta_i(t)$ is the demodulated phase.

The first and second derivatives of $z_i(t)$ are derived as follows:

$$\begin{cases} \dot{z}_i(t) = (\dot{\psi}_i + i\nu_i \psi_i) e^{i\nu_i t} + \text{c.c.}, \\ \ddot{z}_i(t) = (\ddot{\psi}_i + 2i\nu_i \dot{\psi}_i - \nu_i^2 \psi_i) e^{i\nu_i t} + \text{c.c.} \end{cases} \tag{D3}$$

Substituting Eqs. (D2) and (D3) into Eq. (D1), we obtain the equation for ψ,

$$\ddot{\psi}_i + 2i\nu_i \dot{\psi} + \gamma_i \dot{\psi}_i + i\gamma_i \nu_i \psi_i = g_{i-1}\psi_{i-1} + g_i \psi_{i+1}. \tag{D4}$$

As shown in Eq. (C6), $g_i/\nu_i \approx \Omega_i$ and we could rewrite Eq. (D4) as

$$i\dot{\psi}_i + \frac{1}{2\nu_i}\ddot{\psi}_i + \frac{\gamma_i}{2\nu_i}\dot{\psi}_i = -\frac{\gamma_i}{2}\psi_i + \frac{\Omega_{i-1}}{2}\psi_{i-1} + \frac{\Omega_i}{2}\psi_{i+1}. \tag{D5}$$

Equation (D5) denotes that ψ_i varies at differing rates, such as the dissipation rate γ_i and the coupling $\Omega_i/2$. Since $\nu_i \gg \gamma_i, \Omega_i, 1$, the second and third terms on the left can be neglected. Thus, the equations of motion can be analogously mapped into the Schrödinger equations:

$$i\frac{\mathrm{d}}{\mathrm{d}t}\Psi = H_{\mathrm{eff}}\Psi, \tag{D6}$$

where

$$H_{\mathrm{eff}} = \begin{pmatrix} -i\gamma_1/2 & \Omega_1/2 & & \\ \Omega_1/2 & -i\gamma_2/2 & \ddots & \\ & \ddots & \ddots & \ddots \\ & & \Omega_{n-1}/2 & -i\gamma_n/2 \end{pmatrix}. \tag{D7}$$

Equation (D6) characterizes the elastic wave (vibrations) transfer between the coupled resonators.

Consider the dynamics of two coupled resonators, assuming that the resonators are nearly the same, $\gamma_S \approx \gamma_I \approx \gamma$:

$$i\frac{\mathrm{d}}{\mathrm{d}t}\begin{pmatrix}\psi_S \\ \psi_I\end{pmatrix} = \begin{pmatrix} -i\gamma/2 & \Omega/2 \\ \Omega/2 & -i\gamma/2 \end{pmatrix}\begin{pmatrix}\psi_S \\ \psi_I\end{pmatrix}. \tag{D8}$$

The eigenvalue of the effective Hamiltonian is $\lambda_\pm = -i(\gamma/2) \pm \Omega/2$ and the eigenvectors are $\phi_1 =$

$(\sqrt{2}/2, \sqrt{2}/2)^{\mathrm{T}}$ and $\phi_2 = (\sqrt{2}/2, -\sqrt{2}/2)^{\mathrm{T}}$. With the initialization, $\phi(0) = (\psi_S(0), \psi_I(0))^{\mathrm{T}} = (1, 0)^{\mathrm{T}}$,

$$\begin{cases} \psi_S(t) = e^{-\gamma t/2} \cos\left(\dfrac{\Omega t}{2}\right), \\ \psi_I(t) = -ie^{-\gamma t/2} \sin\left(\dfrac{\Omega t}{2}\right). \end{cases} \tag{D9}$$

Therefore, the vibration intensity $|\psi_{S,I}|^2$ is measured:

$$\begin{cases} V_S(t) \propto |\psi_S(t)|^2 = e^{-\gamma t} \cos^2\left(\dfrac{\Omega}{2} t\right), \\ V_I(t) \propto |\psi_I(t)|^2 = e^{-\gamma t} \sin^2\left(\dfrac{\Omega}{2} t\right). \end{cases} \tag{D10}$$

We have conducted Rabi-like oscillations under a linearly changing coupling strength, $g(t) = g_0(1 - t/T)$, $\Omega = \Omega_0(1 - t/T)$, demonstrating the variability of the coupling strength and the rate of oscillations. Consider the Hamiltonian without dissipation, $H'(t)$, with varying coupling $\Omega(t)/2$. Assuming that $\epsilon = \Omega_0/2T$, the solution of the equation

$$i\dot{\Psi} = H'(t)\Psi = \begin{pmatrix} 0 & \epsilon(T-t) \\ \epsilon(T-t) & 0 \end{pmatrix} \Psi \tag{D11}$$

is $\phi_{1,2}(t) = \phi_{1,2}(0)e^{\pm\epsilon(Tt - t^2/2)}$, so we have the amplitude with the dissipation taken into account,

$$\begin{cases} \psi_S = e^{-\gamma t/2} \cos\left(\epsilon\left(\dfrac{t^2}{2} - Tt\right)\right), \\ \psi_I = ie^{-\gamma t/2} \sin\left(\epsilon\left(\dfrac{t^2}{2} - Tt\right)\right). \end{cases} \tag{D12}$$

Thus, the signal intensity is

$$\begin{cases} V_S(t) \propto e^{-\gamma t} \cos^2\left(\dfrac{\Omega_0 t}{2}\left(1 - \dfrac{t}{2T}\right)\right), \\ V_I(t) \propto e^{-\gamma t} \sin^2\left(\dfrac{\Omega_0 t}{2}\left(1 - \dfrac{t}{2T}\right)\right). \end{cases} \tag{D13}$$

[1] P. A. Truitt, J. B. Hertzberg, C. C. Huang, K. L. Ekinci, and K. C. Schwab, Efficient and sensitive capacitive readout of nanomechanical resonator arrays, Nano Lett. **7**, 120 (2007).

[2] J. Doster, T. Shah, T. Fösel, P. Paulitschke, F. Marquardt, and E. M. Weig, Observing polarization patterns in the collective motion of nanomechanical arrays, Nat. Commun. **13**, 2478 (2022).

[3] D. Hatanaka, I. Mahboob, K. Onomitsu, and H. Yamaguchi, Phonon waveguides for electromechanical circuits, Nat. Nanotechnol. **9**, 520 (2014).

[4] J. Cha and C. Daraio, Electrical tuning of elastic wave propagation in nanomechanical lattices at MHz frequencies, Nat. Nanotechnol. **13**, 1016 (2018).

[5] P. Huang, L. Zhang, J. Zhou, T. Tian, P. Yin, C. Duan, and J. Du, Nonreciprocal radio frequency transduction in a parametric mechanical artificial lattice, Phys. Rev. Lett. **117**, 017701 (2016).

[6] P. Rabl, S. J. Kolkowitz, F. H. L. Koppens, J. G. E. Harris, P. Zoller, and M. D. Lukin, A quantum spin transducer based on nanoelectromechanical resonator arrays, Nat. Phys. **6**, 602 (2010).

[7] W. Fon, M. H. Matheny, J. Li, L. Krayzman, M. C. Cross, R. M. D'Souza, J. P. Crutchfield, and M. L. Roukes, Complex dynamical networks constructed with fully controllable nonlinear nanomechanical oscillators, Nano Lett. **17**, 5977 (2017).

[8] M. Zhang, S. Shah, J. Cardenas, and M. Lipson, Synchronization and phase noise reduction in micromechanical oscillator arrays coupled through light, Phys. Rev. Lett. **115**, 163902 (2015).

[9] M. H. Matheny, J. Emenheiser, W. Fon, A. Chapman, A. Salova, M. Rohden, J. Li, M. Hudoba De Badyn, M. Pósfai, L. Duenas-Osorio, M. Mesbahi, J. P. Crutchfield, M. C. Cross, R. M. D'Souza, and M. L. Roukes, Exotic states in a simple network of nanoelectromechanical oscillators, Science **363**, eaav7932 (2019).

[10] F. Molnar, T. Nishikawa, and A. E. Motter, Network experiment demonstrates converse symmetry breaking, Nat. Phys. **16**, 351 (2020).

[11] M. I. N. Rosa, R. K. Pal, J. R. F. Arruda, and M. Ruzzene, Edge states and topological pumping in spatially modulated elastic lattices, Phys. Rev. Lett. **123**, 034301 (2019).

[12] Y. Xia, E. Riva, M. I. N. Rosa, G. Cazzulani, A. Erturk, F. Braghin, and M. Ruzzene, Experimental observation of temporal pumping in electromechanical waveguides, Phys. Rev. Lett. **126**, 095501 (2021).

[13] J. P. Mathew, J. D. Pino, and E. Verhagen, Synthetic gauge fields for phonon transport in a nano-optomechanical system, Nat. Nanotechnol. **15**, 198 (2020).

[14] J. P. Mathew, R. N. Patel, A. Borah, R. Vijay, and M. M. Deshmukh, Dynamical strong coupling and parametric amplification of mechanical modes of graphene drums, Nat. Nanotechnol. **11**, 747 (2016).

[15] X. Zhou, C. Zhao, D. Xiao, J. Sun, G. Sobreviela, D. D. Gerrard, Y. Chen, I. Flader, T. W. Kenny, X. Wu, and A. A. Seshia, Dynamic modulation of modal coupling in microelectromechanical gyroscopic ring resonators, Nat. Commun. **10**, 4980 (2019).

[16] K. Gajo, S. Schüz, and E. M. Weig, Strong 4-mode coupling of nanomechanical string resonators, Appl. Phys. Lett. **111**, 133109 (2017).

[17] Z.-C. Gong, H. Fu, T.-H. Mao, Q. Yuan, C.-Y. Shen, C.-P. Sun, Y. Li, and G.-Y. Cao, Coherent phonon-mediated dynamics for an addressable transducer of coupled micromechanical resonators, Appl. Phys. Lett. **118**, 203505 (2021).

[18] Z.-Z. Zhang, X.-X. Song, G. Luo, Z.-J. Su, K.-L. Wang, G. Cao, H.-O. Li, M. Xiao, G.-C. Guo, L. Tian, G.-W. Deng, and G.-P. Guo, Coherent phonon dynamics in spatially separated graphene mechanical resonators, Proc. Natl. Acad. Sci. USA **117**, 5582 (2020).

[19] T. Faust, J. Rieger, M. J. Seitner, P. Krenn, J. P. Kotthaus, and E. M. Weig, Nonadiabatic dynamics of two strongly coupled nanomechanical resonator modes, Phys. Rev. Lett. **109**, 037205 (2012).

[20] T. Faust, J. Rieger, M. J. Seitner, J. P. Kotthaus, and E. M. Weig, Coherent control of a classical nanomechanical two-level system, Nat. Phys. **9**, 485 (2013).

[21] A. Eichler, M. del Álamo Ruiz, J. A. Plaza, and A. Bachtold, Strong coupling between mechanical modes in a nanotube resonator, Phys. Rev. Lett. **109**, 025503 (2012).

[22] H. Okamoto, A. Gourgout, C.-Y. Chang, K. Onomitsu, I. Mahboob, E. Y. Chang, and H. Yamaguchi, Coherent phonon manipulation in coupled mechanical resonators, Nat. Phys. **9**, 480 (2013).

[23] C. F. Ockeloen-Korppi, E. Damskägg, J. M. Pirkkalainen, M. Asjad, A. A. Clerk, F. Massel, M. J. Woolley, and M. A. Sillanpää, Stabilized entanglement of massive mechanical oscillators, Nature **556**, 478 (2018).

[24] S. Lin, T. Tian, P. Huang, P. Yin, L. Zhang, and J. Du, Realization of programmable nanomechanical lattice with both nearest-neighboring and next-nearest-neighboring couplings, Appl. Phys. Lett. **117**, 093503 (2020).

[25] T. Tian, Y. Ke, L. Zhang, S. Lin, Z. Shi, P. Huang, C. Lee, and J. Du, Observation of dynamical phase transitions in a topological nanomechanical system, Phys. Rev. B **100**, 024310 (2019).

[26] T. Tian, S. Lin, L. Zhang, P. Yin, P. Huang, C. Duan, L. Jiang, and J. Du, Perfect coherent transfer in an on-chip reconfigurable nanoelectromechanical network, Phys. Rev. B **101**, 174303 (2020).

[27] Q. P. Unterreithmeier, E. M. Weig, and J. P. Kotthaus, Universal transduction scheme for nanomechanical systems based on dielectric forces, Nature **458**, 1001 (2009).

[28] A. N. Cleland and M. L. Roukes, External control of dissipation in a nanometer-scale radiofrequency mechanical resonator, Sens. Actuators A: Phys. **72**, 256 (1999).

[29] S. Schmid, K. D. Jensen, K. H. Nielsen, and A. Boisen, Damping mechanisms in high-Q micro and nanomechanical string resonators, Phys. Rev. B **84**, 165307 (2011).

[30] M. J. Seitner, K. Gajo, and E. M. Weig, Damping of metallized bilayer nanomechanical resonators at room temperature, Appl. Phys. Lett. **105**, 213101 (2014).

[31] M. Takamura, H. Okamoto, K. Furukawa, H. Yamaguchi, and H. Hibino, Energy dissipation in graphene mechanical resonators with and without free edges, Micromachines **7**, 158 (2016).

[32] A. Venkatesan, K. J. Lulla, M. J. Patton, A. D. Armour, C. J. Mellor, and J. R. Owers-Bradley, Dissipation in a gold nanomechanical resonator at low temperatures, J. Low Temp. Phys. **158**, 685 (2010).

[33] M. Rossi, D. Mason, J. Chen, Y. Tsaturyan, and A. Schliesser, Measurement-based quantum control of mechanical motion, Nature **563**, 53 (2018).

[34] Y. Tsaturyan, A. Barg, E. S. Polzik, and A. Schliesser, Ultracoherent nanomechanical resonators via soft clamping and dissipation dilution, Nat. Nanotechnol. **12**, 776 (2017).

[35] E. C. Bullard, J. Li, C. R. Lilley, P. Mulvaney, M. L. Roukes, and J. E. Sader, Dynamic similarity of oscillatory flows induced by nanomechanical resonators, Phys. Rev. Lett. **112**, 015501 (2014).

[36] T. Tian, Y. Zhang, L. Zhang, L. Wu, S. Lin, J. Zhou, C.-K. Duan, J.-H. Jiang, and J. Du, Experimental realization of nonreciprocal adiabatic transfer of phonons in a dynamically modulated nanomechanical topological insulator, Phys. Rev. Lett. **129**, 215901 (2022).

[37] X. Chen, I. Lizuain, A. Ruschhaupt, D. Guéry-Odelin, and J. G. Muga, Shortcut to adiabatic passage in two- and three-level atoms, Phys. Rev. Lett. **105**, 123003 (2010).

[38] D. M. Long, P. J. D. Crowley, and A. Chandran, Nonadiabatic topological energy pumps with quasiperiodic driving, Phys. Rev. Lett. **126**, 106805 (2021).

[39] Y. Yang, C. Peng, D. Zhu, H. Buljan, J. D. Joannopoulos, B. Zhen, and M. Soljačić, Synthesis and observation of non-Abelian gauge fields in real space, Science **365**, 1021 (2019).

[40] N. G. Green, A. Ramos, and H. Morgan, Numerical solution of the dielectrophoretic and travelling wave forces for interdigitated electrode arrays using the finite element method, J. Electrostat. **56**, 235 (2002).

[41] R. Chen, R. Liu, and H. Shen, in *2013 IEEE/RSJ International Conference on Intelligent Robots and Systems* (Tokyo, Japan, 2013), p. 2327.

[42] D. J. Griffiths, *Introduction to Electrodynamics* (Pearson, Boston, 2012), 4th ed.

[43] M. Poot and H. S. J. Van Der Zant, Mechanical systems in the quantum regime, Phys. Rep. **511**, 273 (2012).